UNIVERSITY OF CALIFORNIA,

IRVINE

Enhanced Estimation of Battery State of Charge Based on Combination of Simplified Electrochemical Model and Bidirectional Gated Recurrent Unit Network

THESIS

submitted in partial satisfaction of the requirements

for the degree of

MASTER OF SCIENCE

in Chemical and Biomolecular Engineering

by

Quanqun Zhang

Thesis Committee:

Professor Iryna Zenyuk, Chair

Professor Plamen Atanassov

Professor Faryar Jabbari

2022

TABLE OF CONTENTS

LIST OF FIGURES

LIST OF TABLES

ACKNOWLEDGMENTS

I would like to sincerely appreciate my thesis advisor and committee chair. Professor Iryna Zenyuk, who offer me an opportunity to explore in the field of battery model in her group. Without the encouragement and inspiration from Iryna, I will not make progress in research. I would like to cordially appreciate to Professor Joo H. Kim from New York University for giving me some valuable suggestions for my thesis. I would also like to appreciate to Professor Plamen Atanassov and Professor Faryar Jabbari for becoming my thesis committee and providing insightful suggestions on my thesis research.

During the two-year study at the Iryna group, I received helpful advice from my colleagues. Thanks to Adrien Stejer and Dominic Morquecho for providing me the experimental data for the thesis.

Finally, I would like to deeply gratitude to my school, the University of California, Irvine. It provides me with a diverse education. I was fortunate to learn some knowledge related to control and artificial intelligence, which led me to find the interests and future research directions.

ABSTRACT OF THE THESIS

Enhanced Estimation of Battery State of Charge Based on Combination of Simplified Electrochemical Model and Bidirectional Gated Recurrent Unit Network

By

Quanquan Zhang

Master of Science in Chemical and Biomolecular Engineering

University of California, Irvine, 2022

Professor Iryna Zenyuk, Chair

The state of charge (SOC) estimation of lithium-ion battery is a core function of the battery management system, which reflects the remaining charge of the battery and is an important parameter for predicting the remaining driving range of an electric vehicle. The accuracy of the battery SOC estimation depends on the precision of the battery model and the validity of the estimation method. In practice, the complex electrochemical characteristics inside the battery and the dynamic changes of the external environment make it difficult to estimate the battery SOC with high accuracy. To enable high accuracy SOC estimation, this paper proposes a method to estimate battery SOC based on the combination of simplified electrochemical model and Bi-directional gated recurrent unit (Bi-GRU) network. In the model simulation, we compare the simplified electrochemical model, the pseudo-two-dimensional model, and the equivalent circuit model and verify that the simplified electrochemical model is more precise than the equivalent circuit model and less precise than the pseudo-two-dimensional model. In the SOC estimation, we compare our proposed method, ampere

hour integral, particle surface utilization rate based on simplified electrochemical model, and extended Kalman filter based on equivalent circuit model. The results show that the accuracy of SOC estimation based on the proposed method is as high as 99.97% and this method outperforms the other methods studied in this work. This work reveals the important role of data-driven and simplified models in the field of battery cloud digital twin and provides a promising strategy for real-time state estimation for next-generation cell-level battery management systems.

Key Words

Lithium-ion batteries, Simplified electrochemical model, SOC estimation, Bi-directional gated recurrent unit network

Introduction

With the progress of technology, energy and environmental issues are becoming more and more prominent, and development of technologies with low-carbon footprint is gradually becoming a major global trend [1]. Lithium-ion batteries are widely used in electric vehicles and energy storage due to their high specific energy, low self-discharge rate, light weight, and environmental friendliness [2]. Usually, battery packs consist of many individual cells connected by series and parallel structures, what can raise issues such as consistency, safety and performance. Therefore, an advanced battery management system (BMS) is needed to optimize the performance of the battery in use [3]. As one of the most important functions in a BMS, accurate battery state of charge (SOC) estimation can better predict the remaining driving range of an electric vehicle and also avoid overcharge and over-discharge of the battery to prolong the battery life [4][5]. However, the highly nonlinear electrochemical properties inside the battery as well as thermal, aging, and external environmental factors make accurate SOC estimation a challenge. Therefore, battery SOC estimation requires an appropriate battery model and an exact estimation method [6][7].

At present, three types of battery models are often used: mechanistic model, equivalent circuit model, and data-driven model [8]. Mechanistic model is based on first-principle modeling and take into account the physical, electronic, and chemical phenomena in the battery [9]. Mechanistic model is the most accurate and provide deep insight into the internal physical and chemical processes of the battery. The most common mechanistic model is the pseudo-two-dimensional (P2D) model [10]. P2D model contains a large number of partial differential equations and usually require finite element analysis methods to solve them, which is time-consuming and thus does not guarantee real-time response in engineering [11]. To solve this problem, many scholars have developed simplified electrochemical models. The single-particle (SP) model is

the most primitive simplified model, which considers only the open-circuit voltage and the kinetic overpotential. Although the calculation is simple, the oversimplification leads to low accuracy of the model when large current is applied [12]. To make the SP model applicable to high current, the simplified P2D (SP2D) model incorporates liquid-phase potential and solid-phase potential. In fact, there are many different forms of SP2D models, for example, Yuan et al. [13] simplified the mass balance equation by Padé approximation and the charge balance equation by double integration. Equivalent circuit model (ECM) maps the ionic and electric processes inside the cell to a net-work of electric circuit components, such as resistors and capacitors [14]. ECM has a simple structure and a small number of parameters, so the parameters are easy to identify and easy to scale up to pack-level management. However, ECM is generally not very accurate and has a weak interpretation of battery electrochemical and transfer processes [15]. Data-driven model treats the battery as a black-box problem and uses historical or real-time data to monitor and diagnose the battery. It has the advantage of being a good approximation of complex, highly nonlinear battery systems and ignores battery types. However, this approach lacks a full understanding of the battery at the physical level. In addition, being data-driven, it requires a large amount of reliable training data, which makes preliminary experiments costly and time-consuming [16].

There are four widely popular methods for battery SOC estimation: open-circuit voltage, ampere hour integral, model-based solution, and data-driven approach [17]. The open-circuit voltage method uses the relationship between the open-circuit voltage (OCV) and SOC to estimate the SOC of batteries. Although this method is simple, it cannot achieve complete cell resting state in practical applications, and the polarization phenomenon will impact the accuracy of the estimation [18]. The ampere hour integral method, also called coulomb counting method, estimates SOC by accumulating the charged and discharged power. This method is simple and stable in performing calculations. However, the low accuracy of SOC estimation by this method is due to the effects of current sampling error, initial SOC, capacity variation, etc. [19]. Model-based estimation method usually includes Kalman filter (KF) and its derivative optimization filter, particle filter (PF), etc. [20]. For example, Cui et al. [21] used the extended Kalman filter (EKF) based on ECM to estimate the battery SOC. The key idea of the EKF is to linearize the measurement equation using Taylor expansion to improve computational efficiency and make it easy to use. However, the drawback of the EKF

is that it does not take into account the uncertainty that arises during the linearization process, especially when there are large fluctuations of the input, the SOC prediction results will also be unstable accordingly. To avoid the problem of linearization, He et al. [22] used the unscented Kalman filter (UKF) based on ECM to estimate SOC. UKF uses sigma points to describe the statistical properties of the vectors based on the unscented transform (UT transform). This method does not require linearization but may lead to non-convergence of results due to improper selection of sigma points. To improve the SOC accuracy and capture the internal electrochemical state of the cell, Speltino et al. [23] designed an observer based on a simplified electrochemical model using the EKF. However, the reliable identification of electrochemical parameters is still problematic. In recent years, due to the rapid development of artificial intelligence, many studies use data-driven methods to estimate the battery SOC so as to avoid the imprecision of the model. Common data-driven methods include neural networks, support vector machine, deep learning, etc. [24]. Reference [25] used back propagation neural network (BPNN) to predict the battery SOC. The neural network takes the battery current, voltage, temperature, etc. features as input and approximates the battery complex mathematical model by learning itself continuously. However, neural networks tend to fall into local optimum and are slow in convergence. To avoid this challenge, Reference [26] applied support vector regression machine (SVR) to estimate SOC. SVR has a better generalization capability because it uses a structural risk minimization criterion. Due to the kernel function, it approximates well the nonlinear functions. However, considering the large amount of data and time dependence during the actual use of the battery, Reference [27] proposed long short-term memory recurrent neural networks (LSTM-RNN) for SOC estimation and achieved a high accuracy estimation result. Regardless of the data-driven approach, a common problem they all face is the quality of the training data. If the training data contains large noise, then the prediction effect will be greatly affected. To solve this problem, many studies have proposed hybrid methods. The most typical hybrid method is combining filtering and data-driven. Cui et al. [28] proposed a combined SOC estimation method using an improved Bi-directional gated recurrent unit (Bi-GRU) network and UKF. They used UKF to denoise the prediction results of Bi-GRU. The disadvantage of this combination approach is that the rapid response of the estimation results cannot be guaranteed because the algorithm is usually loaded in the cloud. Shin et al. [29] used LSTM to

compensate for the SOC based on the EKF estimator. This combination is not only effective in improving the accuracy of the estimation but also ensures the real-time performance of the estimation results.

Inspired by model-based methods and hybrid compensation structures, this paper proposes a method to estimate the battery SOC based on simplified electrochemical model (SP2D) combined with Bi-directional gated recurrent unit network correction, where the SP2D model uses the simplification method in Reference [13]. We expect the proposed method to be suitable for real-time calculations in the engineering field, which not only effectively improves the accuracy of the estimation but also provides some insight into the internal physical and chemical processes of the cell. **Figure 1** shows the framework of our proposed method. The input of Bi-GRU is the voltage error and current, and the output is the SOC error. Finally, the prediction error is compensated against the SOC error based on the particle surface utilization rate of SP2D. The novelty of this framework has three points. First, the accuracy of SOC estimation can be effectively improved by compensating for electrode-level SOC errors. Second, using a simplified electrochemical model allows monitoring internal electrochemical variables, especially solid and liquid phase concentrations, while estimating SOC. This helps manufacturers to understand the internal changes in the battery during use. Third, leveraging a deep learning algorithm to get rid of the linearization problem in filtering techniques, which allows the model to consider more diverse features and apply to more complex conditions in the future.

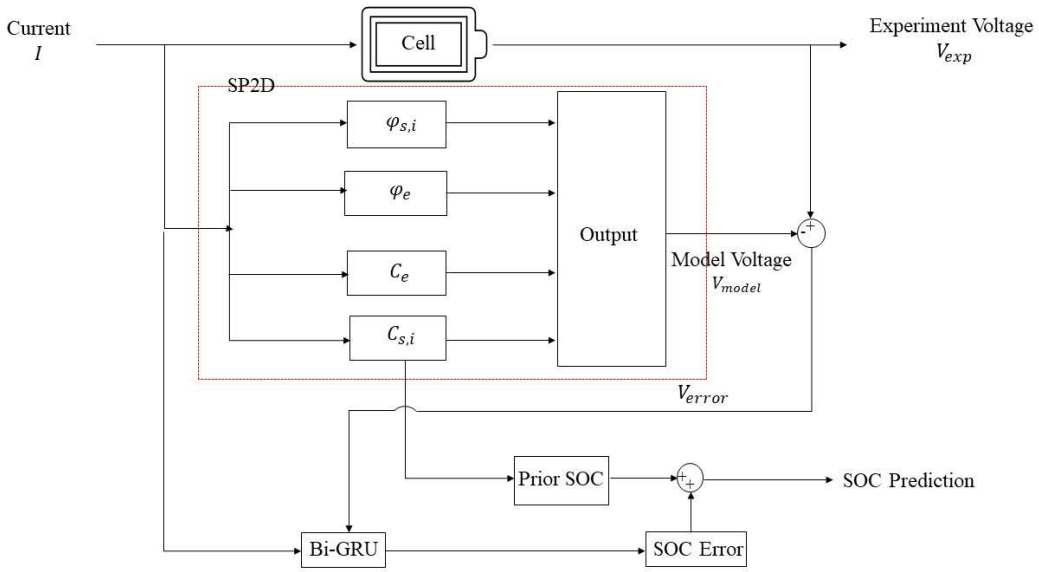

Figure 1. Framework of combining SP2D and Bi-GRU ($\varphi_{s,i}$ and φ_e are respectively the potential of solid phase and liquid phase. C_e and $C_{s,i}$ are respectively the lithium concentration of liquid phase and solid phase. η_i is the kinetic overpotential. The input is the applied current and the output is the predicted SOC of the cell.)

Lithium-ion Battery Operation Principle

Figure 2 shows the geometry of a lithium-ion battery. A lithium-ion battery consists of three parts: anode, cathode and a separator. Generally, the current collector for the anode is copper foil and the current collector for the cathode is aluminum foil. The electrolyte is the connecting substance of the positive and negative electrodes of the battery, which has high ionic conductivity and mainly provides a carrier for the transport of lithium ions between the positive and negative electrodes. During the discharge of Li-ion battery, lithium ions come out of the negative electrode particles, flow into the positive electrode after diffusion and migration in the electrolyte, and are intercalated into the positive electrode particles. At the same time, current in the external circuit flows from the positive electrode to the negative electrode. The discharging process leads to a change in the concentration of lithium ions and also results in a voltage difference between the positive and negative electrodes. The lithium-ion battery charging process is the reverse of the above process. The following electrochemical equations describe the electrochemical reactions of the battery during the charging and discharging process.

Negative：

$$Li_nC_6 \underset{Charge}{\overset{Discharge}{\rightleftharpoons}} C_6 + nLi^+ + ne^-$$

Positive：

$$Li_{m-n}Mn_2O_4 + nLi^+ + ne^- \underset{Charge}{\overset{Discharge}{\rightleftharpoons}} Li_mMn_2O_4$$

Total：

$$Li_{m-n}Mn_2O_4 + Li_nC_6 \underset{Charge}{\overset{Discharge}{\rightleftharpoons}} Li_mMn_2O_4 + C_6$$

Lithium Battery Model

A. pseudo-two-dimensional (P2D) model

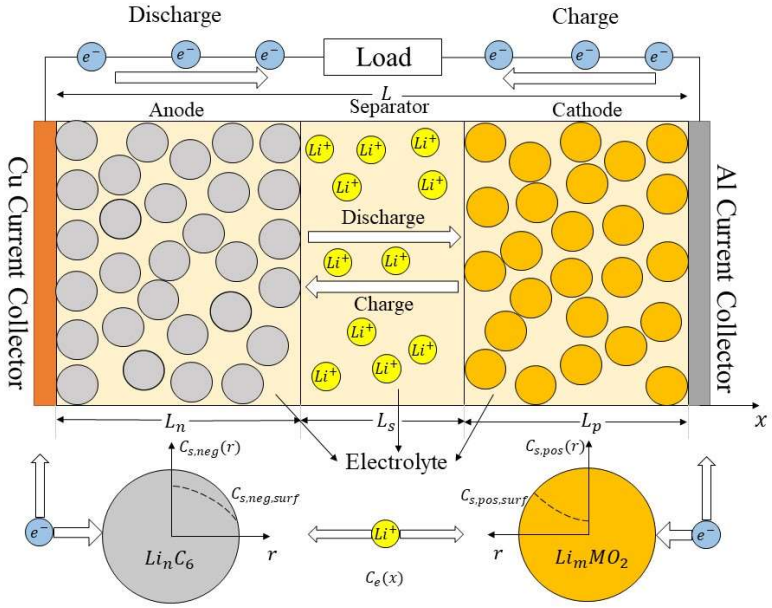

Figure 2. Geometry of lithium battery (L_n, L_s, and L_p are respectively the anode, separator and cathode thickness, L is thickness of the electrodes and separator assembly. The movement direction of electrons and lithium ions is determined by the charge or discharge of the cell.)

Doyle and Newman proposed a pseudo-two-dimensional model based on porous electrode theory and concentrated solution theory [30]. The P2D model describes the two-phase and three-region reaction process inside a lithium-ion battery. In the **Figure 2**, the x-axis is established from the anode to cathode, and the r-axis is established from the inside of the particle to the outside. The geometry thickness and phases are shown in **Table 1**.

Table 1. Thickness and phases of geometry

	Anode	Cathode	Separator
Thickness	L_n	L_p	L_s
Phases	S, L	S, L	L

The P2D model consists of five equations: two mass balance equations, two charge balance equations, and one kinetic equation. The mass and charge governing equations and boundary conditions of the P2D model are summarized in **Table 2** and **Table 3Table 3.** Boundary conditions of the P2D Model. The expressions of all effective parameters in the equations are summarized in **Table 4**.The meanings of all parameters

and variables are presented in Appendix A.

Table 2. Governing equations of the P2D model

Variable	Governing Equation	Eq.	Region
$C_{s,i}$	$\frac{\partial C_{s,i}}{\partial t} = \frac{D_{s,i}}{r^2}\frac{\partial}{\partial r}\left(r^2\frac{\partial C_{s,i}}{\partial r}\right)$	(1)	Anode, Cathode
C_e	$\varepsilon_{e,i}\frac{\partial C_e}{\partial t} = D_{e,i}^{eff}\frac{\partial^2 C_e}{\partial x^2} + (1-t_+)\frac{j_{f,i}}{F}$	(2)	Anode, Separator, Cathode
$\varphi_{s,i}$	$\sigma_i^{eff}\frac{\partial^2 \varphi_{s,i}}{\partial x^2} = j_{f,i}$	(3)	Anode, Cathode
φ_e	$K_i^{eff}\frac{\partial^2 \varphi_e}{\partial x^2} = K_i^{eff}\frac{2RT}{F}(1-t_+)\frac{\partial^2 \ln C_e}{\partial x^2} - j_{f,i}$	(4)	Anode, Separator, Cathode

Table 3. Boundary conditions of the P2D Model

Variable	Boundary Condition	Boundary
$C_{s,i}$	$D_{s,i}\frac{\partial C_{s,i}}{\partial r}\Big\|_{r=0} = 0$	Center of active particle
	$D_{s,i}\frac{\partial C_{s,i}}{\partial r}\Big\|_{r=R_{s,i}} = -\frac{j_{f,i}}{a_{s,i}F}$	Surface of active particle
C_e	$D_{e,neg}^{eff}\frac{\partial C_e}{\partial x}\Big\|_{x=0} = 0$	Current Collector | Negative Electrode
	$D_{e,pos}^{eff}\frac{\partial C_e}{\partial x}\Big\|_{x=L_p+L_s+L_n} = 0$	Positive Electrode | Current Collector
	$D_{e,neg}^{eff}\frac{\partial C_e}{\partial x}\Big\|_{x=L_n^-} = D_{e,sep}^{eff}\frac{\partial C_e}{\partial x}\Big\|_{x=L_n^+}$	Negative | Separator
	$D_{e,sep}^{eff}\frac{\partial C_e}{\partial x}\Big\|_{x=(L_n+L_s)^-} = D_{e,pos}^{eff}\frac{\partial C_e}{\partial x}\Big\|_{x=(L_n+L_s)^+}$	Separator | Positive
	$C_e\|_{x=L_n^-} = C_e\|_{x=L_n^+}$	Negative | Separator
	$C_e\|_{x=(L_n+L_s)^-} = C_e\|_{x=(L_n+L_s)^+}$	Separator | Positive
$\varphi_{s,i}$	$\sigma_{neg}^{eff}\frac{\partial \varphi_{s,neg}}{\partial x}\Big\|_{x=0} = -\frac{I(t)}{A}$	Current Collector | Negative Electrode
	$\sigma_{pos}^{eff}\frac{\partial \varphi_{s,pos}}{\partial x}\Big\|_{x=L_p+L_s+L_n} = -\frac{I(t)}{A}$	Positive Electrode | Current Collector
	$\sigma_{neg}^{eff}\frac{\partial \varphi_{s,neg}}{\partial x}\Big\|_{x=L_n} = 0$	Negative | Separator
	$\sigma_{pos}^{eff}\frac{\partial \varphi_{s,pos}}{\partial x}\Big\|_{x=L_s+L_n} = 0$	Separator | Positive
φ_e	$-K_{neg}^{eff}\frac{\partial \varphi_e}{\partial x}\Big\|_{x=0} = 0$	Current Collector | Negative Electrode
	$-K_{pos}^{eff}\frac{\partial \varphi_e}{\partial x}\Big\|_{x=L_p+L_s+L_n} = 0$	Positive Electrode | Current Collector

	$(K_{neg}^{eff}\frac{\partial\varphi_e}{\partial x}-K_{neg}^{eff}\frac{2RT}{F}(1-t_+)\frac{\partial \ln C_e}{\partial x})\Big\vert_{x=L_n{}^-}$ $=$ $K_{sep}^{eff}\frac{\partial\varphi_e}{\partial x}-K_{sep}^{eff}\frac{2RT}{F}(1-t_+)\frac{\partial \ln C_e}{\partial x})\Big\vert_{x=L_n{}^+}$	Negative | Separator
	$(K_{sep}^{eff}\frac{\partial\varphi_e}{\partial x}-K_{sep}^{eff}\frac{2RT}{F}(1-t_+)\frac{\partial \ln C_e}{\partial x})\Big\vert_{x=(L_n+L_s)^-}$ $=$ $K_{pos}^{eff}\frac{\partial\varphi_e}{\partial x}-K_{pos}^{eff}\frac{2RT}{F}(1-t_+)\frac{\partial \ln C_e}{\partial x})\Big\vert_{x=(L_n+L_s)^+}$	Separator | Positive
	$\varphi_e\vert_{x=L_n{}^-}=\varphi_e\vert_{x=L_n{}^+}$	Negative | Separator
	$\varphi_e\vert_{x=(L_n+L_s)^-}=\varphi_e\vert_{x=(L_n+L_s)^+}$	Separator | Positive

Table 4. Effective parameter

Effective Parameter	Expression	Region
$D_{e,i}^{eff}$	$D_{e,i}^{eff}=D_{e,i}{\varepsilon_{e,i}}^{Brugg}$	Anode, Separator, Cathode
σ_i^{eff}	$\sigma_i^{eff}=\sigma_i{\varepsilon_{s,i}}^{Brugg}$	Anode, Cathode
K_i^{eff}	$K_i^{eff}=K_i{\varepsilon_{e,i}}^{Brugg}$	Anode, Separator, Cathode

The Butler-Volmer equation describes the electrochemical reaction at the interface of the solid-liquid phase in the positive and negative electrodes of lithium batteries, through which the relationship between the overpotential of the particle surface and the volumetric current density can be obtained as follow.

$$j_{f,i}=a_{s,i}Fk_i{C_e}^{\alpha_a}(C_{s,i,max}-C_{s,i,surf})^{\alpha_a}{C_{s,i,surf}}^{\alpha_c}\left[\exp\left(\frac{\alpha_aF\eta_i}{RT}\right)-\exp\left(-\frac{\alpha_cF\eta_i}{RT}\right)\right] \quad (5)$$

where, the kinetic overpotential η_i can be calculated by the following expression.

$$\eta_i=\varphi_{s,i}-\varphi_{e,i}-U_{ocv,i}\left(\frac{C_{s,i,surf}}{C_{s,i,max}}\right) \quad (6)$$

The output voltage of cell is given by

$$V=\varphi_{s,pos}(L)-\varphi_{s,neg}(0) \quad (7)$$

B. Simplified P2D (SP2D) model

The SP2D model is an extended form of the single-particle model. The single particle model uses a single spherical particle to represent the overall properties of the positive and negative active materials. The single-particle model has the output voltage being

related to the open circuit voltage and the overpotential, neglecting the effects of liquid phase concentration, liquid phase potential, and solid phase potential. Because the single-particle model is too simplified, the single-particle model is only suitable for small C-rate and constant current conditions. In order to adapt the model to large C-rate and dynamic conditions, the liquid phase concentration, liquid phase potential and solid phase potential should be added to the single particle model. All parameters in the simplified model are the same as in the P2D model.

1) Simplification of Solid-phase Lithium Diffusion

Since the electrode is a single particle, here we do not need to consider the position of the particle in the electrode. The Laplace transformation of Eq. (1) and the corresponding boundary conditions leads to the following expressions:

$$sC_{s,i}(r,s) = D_{s,i}\frac{d^2C_{s,i}(r,s)}{dr^2} + \frac{2D_{s,i}}{r}\frac{dC_{s,i}(r,s)}{dr} \tag{8}$$

$$D_{s,i}\frac{dC_{s,i}(r,s)}{dr}\bigg|_{r=0} = 0 \tag{9}$$

$$D_{s,i}\frac{dC_{s,i}(r,s)}{dr}\bigg|_{r=R_{s,i}} = -\frac{j_{f,i}(s)}{a_{s,i}F} \tag{10}$$

The transfer function of the particle surface lithium concentration $C_{s,i,surf}(t)$ to the volumetric current density $j_{f,i}(t)$ can be obtained by solving Eq. (8) and using [1, 2] Padé Approximation as follow.

$$\frac{C_{s,i,surf}(s)}{j_{f,i}(s)} = -\frac{\frac{3}{R_{s,i}} + \frac{2}{7}\frac{R_{s,i}}{D_{s,i}}}{a_{s,i}F\left(1 + \frac{1}{35}\frac{{R_{s,i}}^2}{D_{s,i}}s\right)s} \tag{11}$$

2) Simplification of Liquid-phase Lithium Diffusion

For the liquid phase mass balance equation, it has six boundary conditions and three governing equations (negative, separator, and positive) are coupled together, which makes it difficult to solve. In this paper, the modified boundary conditions from Reference [13] are used to solve for the electrolyte lithium concentration. Therefore, the Laplace transformation of Eq. (2) and its boundary conditions leads to the following

equations.

$$s\varepsilon_{e,i}C_e(x,s) = D_{e,i}^{eff}\frac{d^2C_e(x,s)}{dx^2} + (1-t_+)\frac{j_{f,i}(x,s)}{F} \tag{12}$$

$$\left.\frac{dC_e(x,s)}{dx}\right|_{x=0} = 0 \tag{13}$$

$$\left.\frac{dC_e(x,s)}{dx}\right|_{x=L_n} = -\frac{C_e(L_n,s)}{\frac{L_s}{2}+\frac{L_p-L_n}{4}} \tag{14}$$

$$\left.\frac{dC_e(x,s)}{dx}\right|_{x=L} = 0 \tag{15}$$

$$\left.\frac{dC_e(x,s)}{dx}\right|_{x=L_n+L_s} = -\frac{C_e(L_n+L_s,s)}{\frac{L_s}{2}-\frac{L_p-L_n}{4}} \tag{16}$$

The transfer function of the electrolyte concentration $C_e(0,t)$ at $x=0$ to the negative volumetric current density $j_{f,neg}(t)$ can be obtained by solving Eq. (12) and using Padé Approximation:

$$\frac{C_e(0,s)}{j_{f,neg}(s)} = \frac{-3(K-2L_n)^2(1-t_+)}{L_n\varepsilon_{e,neg}\left(-3K^2+10KL_n-10{L_n}^2\right)s+(12K-24L_n)D_{e,neg}^{eff}} \tag{17}$$

where, $K=-2L_s-L_p+L_n$.

Similarly, we can obtain the transfer function of the electrolyte concentration $C_e(L,t)$ at $x=L$ to the positive volumetric current density $j_{f,pos}(t)$:

$$\frac{C_e(L,s)}{j_{f,neg}(s)} = \frac{-3\left(K'+2L_p\right)^2(1-t_+)}{L_p\varepsilon_{e,pos}\left(-3K'^2+10K'L_p+10{L_p}^2\right)s+\left(12K'+24L_p\right)D_{e,pos}^{eff}} \tag{18}$$

where, $K=2L_s-L_p+L_n$.

3) Simplification of Liquid-phase Charge Balance Equation

Since the liquid phase concentration C_e and the liquid phase potential φ_e in Eq. (4) and its boundary conditions are only derived with respect to the position variable$x$, but not the time variable t, here we use the method of double integration and thus removing the second order differential form.

In the anode part, Eq. (4) can be simplified by applying double integration of x from 0 to L_n and boundary conditions.

Then, the liquid phase potential difference between $x = 0$ and $x = L_n$ is expressed as

$$\varphi_e(L_n, t) - \varphi_e(0, t) = \frac{2RT(1 - t_+)}{FC_{e,0}}[C_e(L_n, t) - C_e(0, t)] - \frac{I(t)}{2AK_{neg}^{eff}}L_n \quad (19)$$

Using the same method to simplify the liquid phase potential in separator (from $x = L_n$ to $x = L_n + L_s$) and cathode (from $x = L_n + L_s$ to $x = L$). Then, the corresponding liquid phase potential difference are expressed as:

$$\varphi_e(L_n + L_s, t) - \varphi_e(L_n, t) = \frac{2RT(1 - t_+)}{FC_{e,0}}[C_e(L_n + L_s, t) - C_e(L_n, t)] - \frac{I(t)}{AK_{sep}^{eff}}L_s \quad (20)$$

$$\varphi_e(L, t) - \varphi_e(L_n + L_s, t) = \frac{2RT(1 - t_+)}{FC_{e,0}}[C_e(L, t) - C_e(L_n + L_s, t)] - \frac{I(t)}{2AK_{pos}^{eff}}L_p \quad (21)$$

So, the overall liquid phase potential difference $\varphi_e(L, t) - \varphi_e(0, t)$ can be expressed as:

$$\frac{2RT(1 - t_+)}{FC_{e,0}}[C_e(L, t) - C_e(0, t)] - \frac{I(t)}{2A}\left(\frac{L_n}{K_{neg}^{eff}} + \frac{2L_s}{K_{sep}^{eff}} + \frac{L_p}{K_{pos}^{eff}}\right) \quad (22)$$

4) Simplification of Solid-phase Charge Balance Equation

The solid phase charge balance equation (Eq. (3)) (3)can also be simplified by applying double integration of x in the anode and cathode. Then, the solid phase potential difference of anode and cathode are described as:

$$\varphi_s(x, t)|_{x=L} - \varphi_s(x, t)|_{x=L_n+L_s} = -\frac{I(t)}{2A}\frac{L_p}{\sigma_{pos}^{eff}} \quad (23)$$

$$\varphi_s(x, t)|_{x=L_n} - \varphi_s(x, t)|_{x=0} = \frac{I(t)}{2A}\frac{L_n}{\sigma_{neg}^{eff}} \quad (24)$$

5) Simplification of Butler-Volmer Equation

Since the Butler-Volmer equation does not contain a differential form, here we simply take out the kinetic overpotential mention η_i and obtain its expression as follow.

$$\eta_i = \frac{RT}{\alpha F}\ln\left(\beta_i + \sqrt{(\beta_i)^2 + 1}\right) \tag{25}$$

where, $\beta_i = \frac{j_{f,i}}{2i_{0,i}}$.

6) Volumetric Current Density

$$j_{f,neg} = \frac{I(t)}{AL_n} \tag{26}$$

$$j_{f,sep} = 0 \tag{27}$$

$$j_{f,pos} = -\frac{I(t)}{AL_p} \tag{28}$$

Ultimately, the output voltage of the cell can be expressed as:

$$\begin{aligned} V(t) = U_{pos}(\theta_{pos}) - U_{neg}(\theta_{neg}) + \frac{RT}{\alpha F}\ln\left(\frac{\beta_{pos} + \sqrt{(\beta_{pos})^2 + 1}}{\beta_{neg} + \sqrt{(\beta_{neg})^2 + 1}}\right) \\ + \frac{2RT(1 - t_+)}{FC_{e,0}}[C_e(L,t) - C_e(0,t)] \\ - \frac{I(t)}{2A}\left(\frac{L_n}{K_{neg}^{eff}} + \frac{2L_s}{K_{sep}^{eff}} + \frac{L_p}{K_{pos}^{eff}}\right) - \frac{I(t)}{2A}\left(\frac{L_p}{\sigma_{pos}^{eff}} + \frac{L_n}{\sigma_{neg}^{eff}}\right) \end{aligned} \tag{29}$$

where, electrode surface utilization rate $\theta_i = \frac{C_{s,i,surf}}{C_{s,i,max}}$.

C. Equivalent Circuit Model (ECM)

The modeling idea of the ECM is mainly based on using the electrical components to equate the electrochemical reactions that occur inside the cell. The ECM has a variety of structural forms, of which the second-order Thevenin model is the most widely used [31]. **Figure 3** shows the second-order Thevenin model of the cell system. Generally speaking, the first RC step ($R_{p1}||C_{p1}$) represents the kinetic polarization, which reflects the double layer structure of the interface between electrode and electrolyte. The second RC step ($R_{p2} \parallel C_{p2}$) represents the concentration polarization, which describes concentration difference between the electrode surface and the reactants or products of the electrolyte bulk. R_0 represents ohmic polarization, which refers to the combination of resistance from charge transfer, electron flow and contact between components.

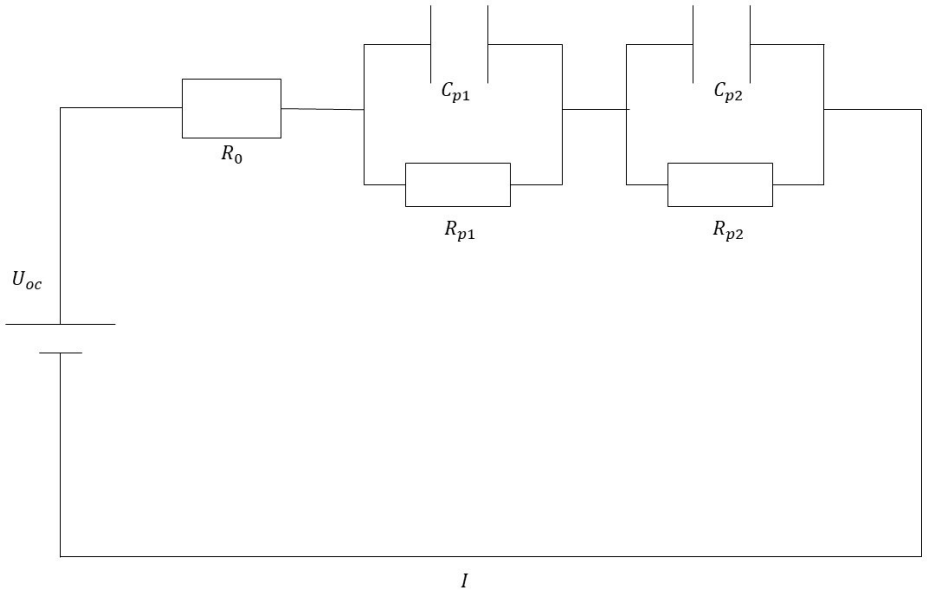

Figure 3. Equivalent Circuit Model (U_{oc} is the open circuit voltage of the cell, I is the external current, R_0 is the ohmic internal resistance, R_{p1} and R_{p2} are polarization resistance, C_{p1} and C_{p2} are polarization capacitance. U_1 and U_2 are respectively the voltage of the first RC step and the second RC step.)

According to ohm's Law, the state equation of the model can be described as

$$\begin{bmatrix} \frac{dU_1}{dt} \\ \frac{dU_2}{dt} \end{bmatrix} = \begin{bmatrix} \frac{-1}{R_{p1}C_{p1}} & 0 \\ 0 & \frac{-1}{R_{p2}C_{p2}} \end{bmatrix} \times \begin{bmatrix} U_1 \\ U_2 \end{bmatrix} + \begin{bmatrix} \frac{1}{C_{p1}} \\ \frac{1}{C_{p2}} \end{bmatrix} \times I(t) \tag{30}$$

$$\begin{bmatrix} y_1 \\ y_2 \end{bmatrix} = \begin{bmatrix} 1 & 0 \\ 0 & 1 \end{bmatrix} \times \begin{bmatrix} U_1 \\ U_2 \end{bmatrix} + [0] \times I(t) \tag{31}$$

The cell output voltage can be expressed as:

$$V(t) = U_{oc} - U_1 - U_2 - R_0 I(t) \tag{32}$$

Method of Battery State of Charge Estimation

A. Ampere Hour Integral

The ampere hour integral method is the most common method for battery SOC estimation, and it has the advantage of being easy to calculate. The weakness is that the ampere hour integral method regards the battery as a black box, it has no explanation

for the battery physical mechanisms and internal changes, and it only considers the current and coulombic efficiency. Besides, the error of the estimated SOC of this method will increase with time. The expression for the SOC is as follow:

$$SOC(t) = SOC_0 - \frac{\eta \int_0^t Idt}{Q_c} \tag{33}$$

where, SOC_0 is the battery initial SOC; η is the columbic coefficient; Q_c is the battery nominal capacity.

B. ECM-based Extended Kalman Filter (EKF)

Extended Kalman filter is a popular method to realize nonlinear state prediction currently. The merit of this method is that it can well solve the nonlinear relationship between the open-circuit voltage and SOC of the battery. In addition, the filter makes the system covariance decrease, thus the error of the predicted SOC is controlled within a certain range. However, for the battery model, the ECM is still weak in explaining the internal phenomenon of the battery. Besides, the stability of the prediction results is affected due to the Jacobi matrix. The discrete state space equations can be obtained by solving the linear system equations of ECM (Eq. (30) and Eq. (31)) as follows:

$$\begin{bmatrix} U_1(k+1) \\ U_2(k+1) \\ SOC(k+1) \end{bmatrix} = \begin{bmatrix} e^{-\frac{T}{R_{p1}C_{p1}}} & 0 & 0 \\ 0 & e^{-\frac{T}{R_{p2}C_{p2}}} & 0 \\ 0 & 0 & 1 \end{bmatrix} \times \begin{bmatrix} U_1(k) \\ U_2(k) \\ SOC(k) \end{bmatrix} + \begin{bmatrix} R_{p1}\left(1 - e^{-\frac{T}{R_{p1}C_{p1}}}\right) \\ R_{p2}\left(1 - e^{-\frac{T}{R_{p2}C_{p2}}}\right) \\ -\frac{\eta T}{Q_c} \end{bmatrix} I_k + w_k \tag{34}$$

The discrete output equation can be expressed as:

$$V_k = U_{ocv}(k) - U_1(k) - U_2(k) - R_0 I_k + v_k \tag{35}$$

where, w_k is system noise, v_k is measurement noise. So, the system variance $Q = IE[w_k {w_k}^T]$ and the measurement variance $R = IE[v_k {v_k}^T]$.

By linearization, we define the discrete state equation and discrete output equation are as follows:

$$X_{k+1} = A_k X_k + B_k I_k + w_k \tag{36}$$

$$V_k = C_k X_k + D_k I_k + v_k \tag{37}$$

Where, $X_k = [U_1(k) \quad U_2(k) \quad SOC(k)]^T$, The expressions of the coefficients of the equations are as follows.

$$A_k = \begin{bmatrix} e^{-\frac{T}{R_{p1}C_{p1}}} & 0 & 0 \\ 0 & e^{-\frac{T}{R_{p2}C_{p2}}} & 0 \\ 0 & 0 & 1 \end{bmatrix} B_k = \begin{bmatrix} R_{p1}(1 - e^{-\frac{T}{R_{p1}C_{p1}}}) \\ R_{p2}(1 - e^{-\frac{T}{R_{p2}C_{p2}}}) \\ -\eta T/Q_c \end{bmatrix}$$

$$C_k = \begin{bmatrix} -1 & -1 & \left.\frac{dU_{ocv}}{dSOC}\right|_{SOC(k+1|k)} \end{bmatrix} D_k = [-R_0]$$

Then, we apply the extended Kalman filter to estimate the battery SOC. the following are the steps of the EKF algorithm.:

1) Filter Initialization

$$X_{0|0} = IE[X_0], \quad P_{0|0} = IE\left[(X_0 - X_{0|0})(X_0 - X_{0|0})^T\right] \tag{38}$$

Where X_0 is the initial state, $P_{0|0}$ is initial system covariance. The precision of X_0 and $P_{0|0}$ has little effect on the accuracy of the state estimation. This is because the EKF algorithm uses the error between the system measurement and the output value to correct for the initial error in the state value, so that it can quickly eliminate the error and stabilize the predicted state around the true value.

2) State Variable and Covariance Prediction

$$X_{k+1|k} = A_k X_{k|k} + B_k I_k \tag{39}$$

$$P_{k+1|k} = A_k P_{k|k} {A_k}^T + Q \tag{40}$$

3) Kalman Gain Update

$$K_{k+1|k} = \frac{P_{k+1|k} {C_k}^T}{C_k P_{k+1|k} {C_k}^T + R} \tag{41}$$

4) State Variable and Covariance Update

$$X_{k+1|k+1} = X_{k+1|k} + K_{k+1|k}\left[V_{k+1} - V_{k+1|k}\right] \tag{42}$$

$$P_{k+1|k+1} = \left[1 - K_{k+1|k} C_k\right] P_{k+1|k} \tag{43}$$

By constantly predicting and updating the state matrix in the time domain, we can obtain the estimated SOC of the battery at each sampling period, meanwhile, the system covariance decreases and stays around a stable value.

C. SP2D-based Particle Surface Utilization Rate

During cell charge and discharge, lithium ions diffuse between the positive and negative electrodes through the electrolyte, and at the same time, lithium ions de-intercalation and intercalation occurs continuously on the positive and negative active material particles. In this process, the lithium concentration on the particle surface will change, so the cell SOC can be defined as a function of the surface utilization rate of the cathode particles θ_{pos}, which is expressed as follow:

$$SOC(t) = \frac{\theta_{pos}(t) - \theta_{pos,0\%}}{\theta_{pos,100\%} - \theta_{pos,0\%}} \tag{44}$$

where, $\theta_{pos,0\%}$ and $\theta_{pos,100\%}$ are the surface utilization rate of positive particles after the battery is fully discharged and fully charged, respectively.

D. SP2D-based Bi-directional Gated Recurrent Unit (Bi-GRU) Correction

Since the battery operation is affected by C-rate, thermal effect, aging effect and external environment, which makes either model will not reflect the real situation of battery operation very well. In particular, in this paper, we only study the electrical model and do not introduce the thermal and aging models, so the internal parameters of the battery will be changed by these influencing factors, which in turn leads to inaccurate SOC estimation. To solve this problem, we propose a SOC correction method. The principle is to use Bi-GRU to predict the error between the estimated SOC of the SP2D model (Prior SOC) and the real SOC of the cell in each sampling cycle, and then output the final estimated cell SOC after compensating this error to the Prior SOC. So, the expression of the cell SOC is as follow.

$$SOC(t) = Prior\ SOC(t) + Prediction\ SOC\ Error(t) \tag{45}$$

Cell SOC is a time-dependent state variable, so it is better to use a time-series algorithm in deep learning for SOC correction. Recurrent neural network (RNN) is a typical time-series algorithm that uses the idea of weight sharing, which makes it possible to greatly reduce the number of parameters at the time scale. However, the cumulative multiplication of weights in RNN at long time scales leads to gradient disappearance or gradient explosion and severely degrades the performance and prediction accuracy of the algorithm. However, the problem of gradient disappearance or gradient explosion in long sequences can be effectively solved by introducing the idea of gating in long

short time memory recurrent neural network (LSTM-RNN) and gated recurrent unit network (GRU). In this work, we prefer to use GRU because GRU has fewer parameters and is easier to train. In the field of computer science, a typical application of the time-series problem is natural language processing (NLP). Generally, the computer needs to combine the text above and the text below to determine the semantics, which will improve the accuracy of prediction. In this paper, we transfer this idea to the battery control domain and use Bi-directional GRU to predict the cell SOC error, which will improve the SOC prediction accuracy.

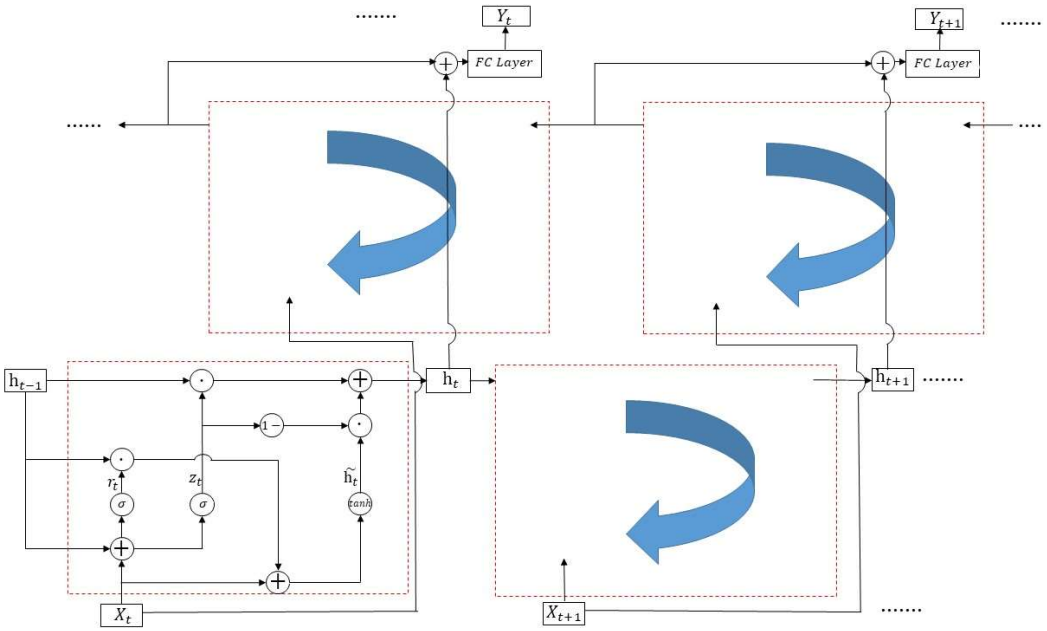

Figure 4. Bi-GRU (+ represents concatenate. · represents the multiplication of the corresponding elements of two matrices. σ and tanh represent the Sigmoid and Tanh activation functions, respectively. $FC\ Layer$ represents the fully connected layer. X_t is the input of the algorithm. h_t is the hidden state, and its practical meaning is the output of each cell. Y_t is the output of the algorithm)

The architecture of a typical Bi-directional gated recurrent unit (Bi-GRU) is shown in **Figure 4**. The two features selected in this paper are the current I and voltage error ΔV, The output is the SOC error of the cell at each moment. Our choice of these two features was inspired by the Kalman filter, which uses the difference between measured and predicted voltages to compensate for the predicted state based on the previous moment. However, due to the linearization, the output is unstable and less accurate. Therefore, we choose the same features as the Kalman filter to train Bi-GRU, expecting to eliminate the downside effects of linearization. The structure of Bi-GRU consists of a

reset gate and an update gate in each cell.

1) Reset gate r_t: To control whether the computation of the candidate state $\widetilde{h_t}$ depends on the previous moment state h_{t-1}

$$r_t = Sigmoid(W_r X_t + U_r h_{t-1} + b_r) \tag{46}$$

$$\widetilde{h_t} = Tanh(W_h X_t + U_h(r_t \cdot h_{t-1}) + b_h) \tag{47}$$

2) Update gate z_t: Control how much information the current state h_t needs to retain from the previous moment state h_{t-1} (without nonlinear transformation) and how much information it needs to accept from the candidate state $\widetilde{h_t}$

$$z_t = Sigmoid(W_z X_t + U_z h_{t-1} + b_z) \tag{48}$$

$$h_t = z_t \cdot h_{t-1} + (1 - z_t) \cdot \widetilde{h_t} \tag{49}$$

where, the function expressions for Sigmoid and Tanh are as follows:

$$Sigmoid(x) = \frac{1}{1 + e^{-x}} \tag{50}$$

$$Tanh(x) = \frac{e^{x} - e^{-x}}{e^{x} + e^{-x}} \tag{51}$$

Since the output of the algorithm contains only one feature, a fully connected layer is needed at each moment, thus enabling the dimensional transformation. What is important to note for both training and testing dataset of the algorithm is that the input is a sequence, and the prediction value is the output of the last moment in this sequence. For example, if the length of sequence is 1000, then the SOC correction of the cell should start from the 1000th moment. In this work, the parameters of the algorithm are as follows: the length of sequence is 2043; the hidden size is 64; the number of layers is 3; the hidden size in the fully connected layers are 32, 8, 2, and 1, respectively; and the epoch is 200.

Results and Discussion

I. Validation of the simplification effect

The voltage comparison between SP2D and P2D models under 1 C pulse charge and discharge cycle is shown in **Figure 5**. In this simulation, the cell is subjected to: 1) discharge at 1 C for 2000 s; 2) rest for 300 s; 3) charge at 1 C for 2000 s; and 4) rest to

8000 s. All parameters are the same as the 1D isothermal lithium-ion battery case in COMSOL Multiphysics 6.0. P2D model was simulated using COMSOL Multiphysics 6.0, and the SP2D model was simulated using Simulink. The overall trend of voltage profiles from two models is similar, but there are still minor observable differences. **Figure 6** shows the relative standard deviation (RSD) of the SP2D model compared to the P2D model. As can be clearly seen, there are four distinct peak points in this figure. The significance of the peak point is that the error caused by the simplification increases suddenly at this moment and then decreases immediately. The time corresponding to these four peak points are 4 s, 2009 s, 2314 s, and 4305 s. Therefore, it can be determined that the phases of severe distortion of the SP2D model come from the initial stage of discharge, the initial stage of rest after discharge, the initial stage of charge, and the initial stage of rest after charge. respectively. **Figure 7** shows the mean relative standard deviation (MRSD) of the SP2D model at different periods. Where Rest 1 and Rest 2 represent the 300 s rest after discharge and charge, and Rest 3 represents the rest from 4600 s to 8000 s. It can be seen that Rest 1 and Rest 2 period have larger MRSD, Discharge and Charge period have smaller and almost the same MRSD. So, we conclude that the SP2D model can accurately simulate the charge and discharge behavior of the cell, but it cannot model the short term of the rest period after charge or discharge with high accuracy. Further analysis of the 300 s rest period shows that the ohmic and kinetic polarization disappear instantaneously at the moment when the applied current is zero, and then the concentration polarization decreases to zero gradually during the remaining rest time because it is not related to the current. Concentration polarization depends on the electrolyte concentration and is a changing state variable over longer time periods. Hence, we deduce that the reason for the large MRSD of the SP2D model in Rest 1 and Rest 2 is the weak capability of simulating the mass transport polarization voltage. Combining the Voltage RSD curve, we find that the worst performance of the SP2D model comes from the concentration relaxation stage.

In order to further investigate the essential cause of the local distortion of the SP2D model, the key variables in the electrochemical model need to be visualized. According to Eq.(29), the cell output voltage is equal to the sum of the open-circuit voltage and the polarization voltage. Generally, the open-circuit voltage is the main contribution to the output voltage. The open-circuit voltages for positive and negative electrodes are

functions of the particle surface lithium concentration. As a result, the first key variable $C_{s,i,surf}$ needs to be visualized. The polarization voltage is composed of kinetic polarization, ohmic polarization and concentration polarization. For both P2D and SP2D models, all three polarizations are a function of the liquid phase lithium concentration. Therefore, the second key variable to be visualized is C_e. In summary, $C_{s,i,surf}$ and C_e versus time for the two models are plotted in **Figure 8** and **Figure 9**. There are two major observations. First, since the electrode in the P2D model is not a single particle, the selected positive particle surface concentration of P2D model is located at half of the positive electrode ($x = L_n + L_s + L_p/2$) and the selected negative particle surface concentration of P2D model is located at half of the negative electrode ($x = L_n/2$). Second, for the variable C_e , two boundary liquid-phase lithium concentrations $C_e(L)$ and $C_e(0)$ should be selected because only the boundary liquid-phase lithium concentration needs to be considered in the output voltage equation of the SP2D model (Eq. (29)). Let's take a look at the anode part as an example. During the discharge period, lithium is de-intercalated from the anode particles and diffuses into the electrolyte, resulting in a decrease in the surface lithium concentration of the particles and an increase in the electrolyte lithium concentration. In the discharge rest period, the applied current of the cell is zero and the surface concentration of the particles increases, which indicates that the simplified model can preserve the physical characteristics and has the benefit of estimating the cell SOC. If we use the Ampere Hour Integration method, the SOC of the cell stays the same when current is zero. However, the electrode-level of the SP2D model for estimating the SOC has a better prediction capability. Accordingly, the electrolyte lithium concentration decreases in this period. During the charging period, the lithium is continuously intercalated into the anode particles from the electrolyte, which leads to an increase in the surface lithium concentration of the particles and a decrease in the lithium concentration of the electrolyte. In the charging rest period, the lithium concentration on the surface of the particles decreases and the electrolyte lithium concentration increases. When the cell is at complete rest, both solid and liquid phase lithium concentrations remain constant. At the cathode, the particle surface lithium concentration and the electrolyte lithium concentration trends are opposite to those of the anode. However, it has to be mentioned that the surface lithium concentration of the positive particles in the P2D model increases slightly during the discharge rest period, which is related to the Li interactions

between the particles. This also indicates that the particles are more densely packed and have stronger interactions at $x = L_n + L_s + L_p/2$. Although from **Figure 8** and **Figure 9** it can be seen that the overall trend of electrolyte lithium concentration and particle surface lithium concentration is the same for both models, there are still local differences. In particular, for the SP2D model positive electrolyte salt concentration profile, it has a significant error compared to the P2D model, which verifies the previous conclusion that the worst performance of the SP2D model comes from the concentration relaxation period. We analyze that the local differences in the two plots are mainly caused by three reasons. First, the Li-ion pore wall flux in the P2D model is constantly changing, while the SP2D model uses a constant average Li-ion pore wall flux. Second, this paper uses a low order of Padé Approximation to reduce the complexity of the system, which leads to a certain degree of distortion in the variables. Third, since the input current is discrete, the transfer function in the s domain needs to be discretized in the simulation, which will further result in the inaccuracy of the governing equations.

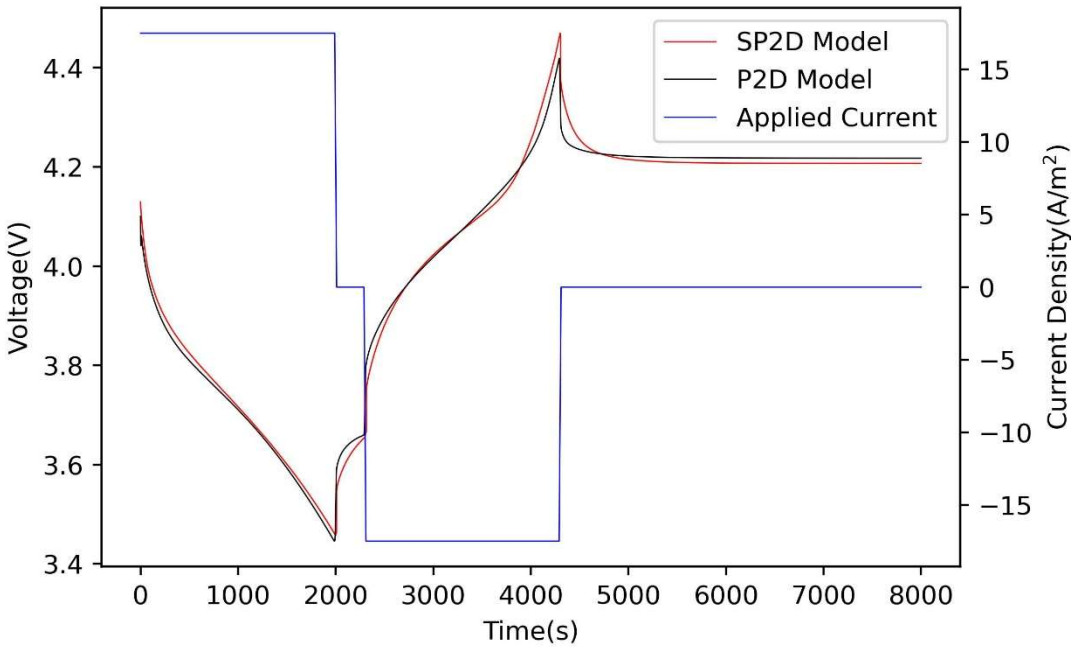

Figure 5. P2D model and SP2D model simulation of cell voltage (left y-axis) and of current density (right y-axis) as a function of time under 1 C-rate.

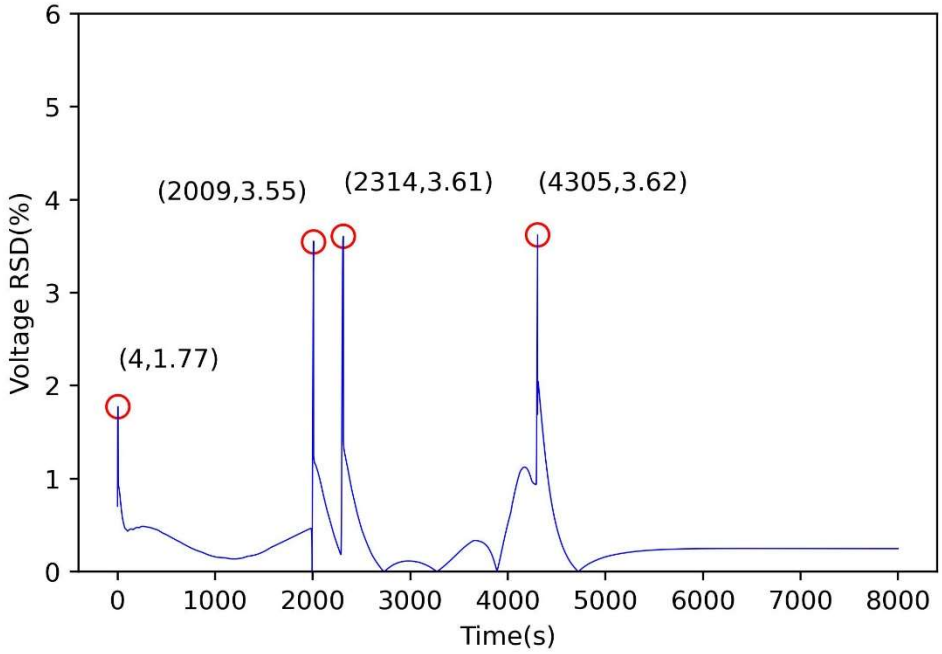

Figure 6. Relative standard deviation of SP2D model compared to P2D model. The time corresponds to the same time as in Figure 5.

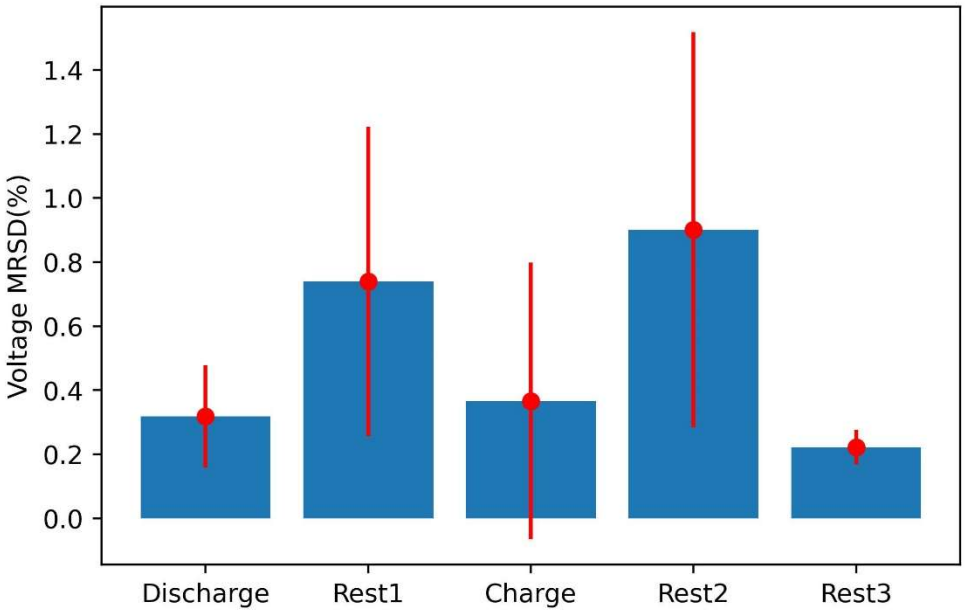

Figure 7. Mean relative standard deviation (MRSD) of voltage of SP2D model compared to P2D model during charge, discharge and rest periods.

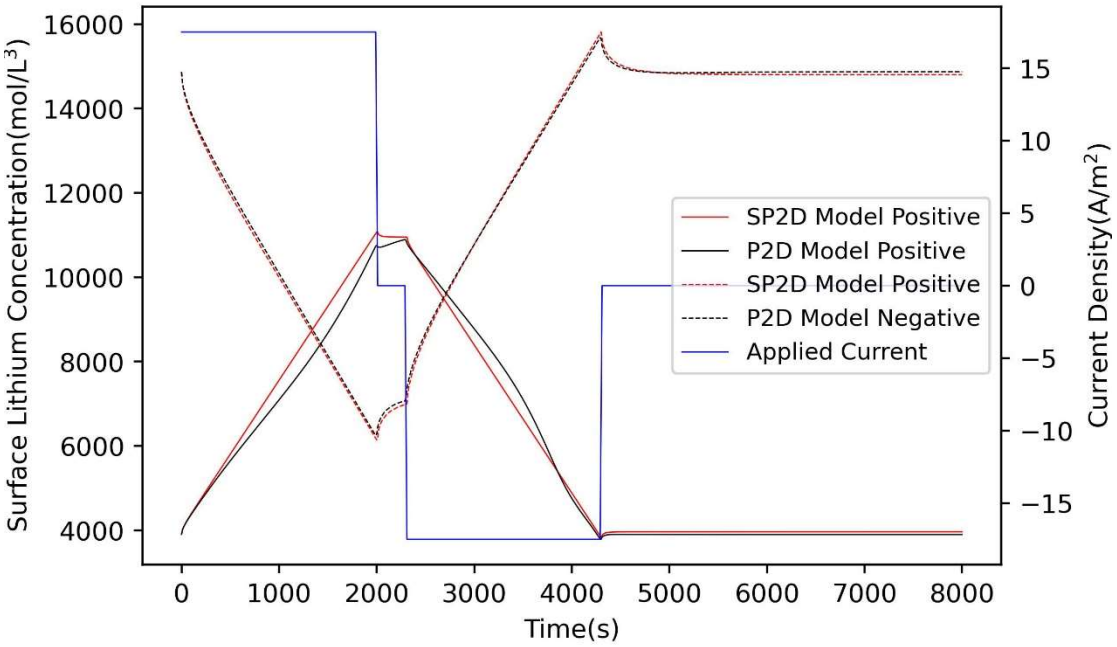

Figure 8. Particle surface lithium concentration as a function of time, where results of SP2D and P2D models are compared. The time corresponds to the same time as in Figure 5. The applied current corresponds to the same current as in Figure 5.

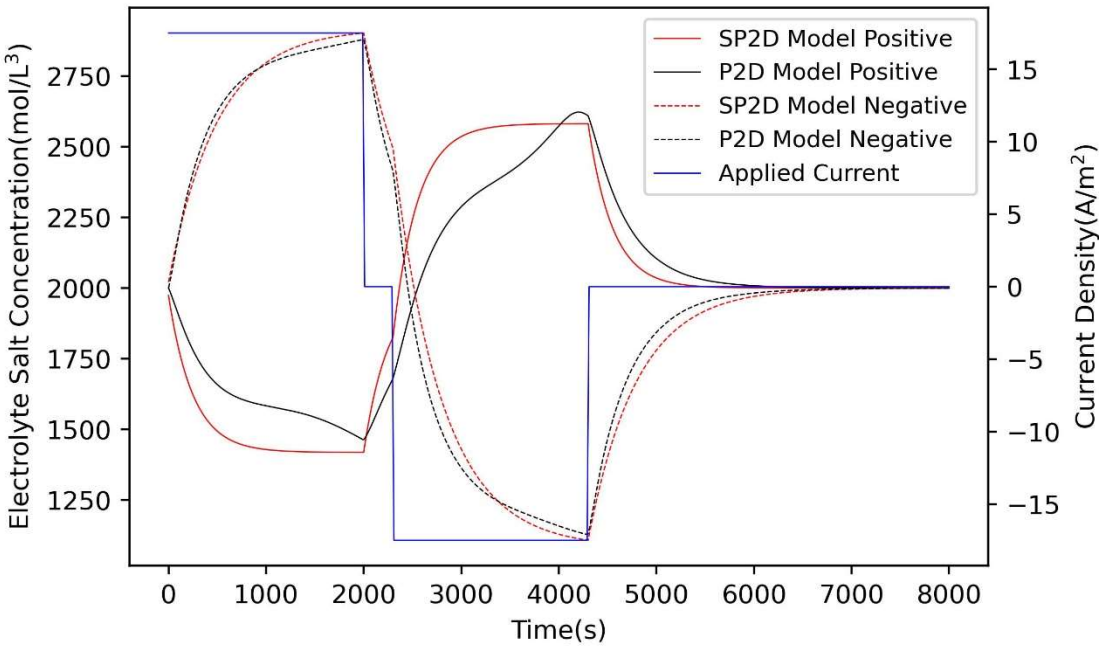

Figure 9. Electrolyte salt concentration as a function of time for SP2D and P2D models. The time corresponds to the same time as in Figure 5. The applied current corresponds to the same current as in Figure 5.

II. Model Comparison

In this section, we compare the P2D model, SP2D model, ECM with experiment (EXP) data. Some electrochemical parameters are derived from Reference [32]. Some electrochemical parameters are adjusted by measurement and matching the P2D model with the experiment data. The resistance and capacitance of ECM are calculated by the relationship between electrical and electrochemical parameters as mentioned in Reference [33]. All parameter values are summarized in **Table 5** and **Table 6**. The cell used in the experiment is a 3.01 mAh lithium manganate (LMO) coin cell. The cell was tested under 0.1 C, 0.2 C, 0.5 C, 1 C and 2 C discharge conditions. The discharge curves for the three models and experiments at five C-rates are shown in **Figure 10**, and the Root Mean Square Error (RMSE) between each model and the experiment data is shown in **Figure 11**. It is clear that the RMSE of the three models grow as the C-rate increases, which means that the prediction capability of all models decreases. By comparison, the ECM error increases significantly because the capability of the ECM for evaluating polarization loss is magnified when the current increases. Although the P2D and SP2D models can theoretically model the polarization voltage accurately, they still cannot fit the experiment data very well at large C-rates. For the P2D model, the reason for this problem is that we do not adjust the parameters with high accuracy, so the effect of parameter uncertainty is amplified at large currents. The P2D model is complex and has a large number of parameters that are difficult to estimate. Accurate parameter identification requires a large number of experiments, precise experimental setups for specific parameter measurements and advanced algorithms to computationally estimate them. For the SP2D model, in addition to the parameter uncertainty, the concentration gradient in solid and liquid phases becomes significant at high currents, which questions the validity of the simplification method and Padé Approximation. It can be seen from **Figure 11** that the RMSE of the SP2D model is larger than that of the P2D model and smaller than that of the ECM at each discharge C-rate, which verifies that the SP2D model is more accurate than the ECM, but less accurate than the P2D model.

Interesting observations is that at 0.1 C-rate, the ECM looks better than the SP2D model except for the high depth-of-discharge (DOD) region. This phenomenon is explainable. When small current is applied, the polarization loss is not significant in the low and medium DOD regions and the output voltage of the cell is almost the same as the open

circuit voltage. At this stage, the solid-phase concentration governing equation in the SP2D model suffers from simplification and inaccuracy of the electrochemical parameters resulting in a slight reduction in the accuracy of the particle surface concentration, which in turn affects the open-circuit voltage. However, the open-circuit voltage of the ECM is more accurate because it is directly calibrated based on the DOD. Therefore, the ECM is more accurate than the SP2D until approximately 30,000 s. However, in the high DOD region, where the concentration polarization is significant, the ECM cannot continue to predict the output voltage accurately, and the SP2D model is more precise the ECM at this point. Next, we compare the rate capabilities of the three models. In **Figure 12**, it is easy to find that both the SP2D model and the P2D models reflect the cell's rate capability very well and can predict the final discharge capacity. However, the ECM does not capture the cell's rate capability because the resistance and capacitance do not vary with the SOC in this paper. If we want the ECM to have a better evaluation of respond voltage, in future we need to add more RC steps to the model architecture and design Hybrid Pulse Power Characteristic (HPPC) experiment to calibrate the relationship between resistance and capacitance with SOC.

Table 5. Parameters for cell electrochemical model

Symbol	Units	Negative Electrode	Separator	Positive Electrode
$D_s{}^f$	$m^2 \cdot s^{-1}$	3.9×10^{-14}	—	1×10^{-13}
$R_s{}^a$	m	2.5×10^{-6}	—	0.8×10^{-6}
$\varepsilon_s{}^a$	—	0.238	—	0.224
$\varepsilon_e{}^a$	—	0.590	0.724	0.517
$C_{e,0}{}^f$	$mol \cdot m^{-3}$	2000	2000	2000
$C_{s,max}{}^a$	$mol \cdot m^{-3}$	52932	—	22860
$C_{s,0}{}^a$	$mol \cdot m^{-3}$	38516	—	4946.1
σ^f	$S \cdot m^{-1}$	100	—	3.8
k^a	$mol^{-1/2} \cdot m^{5/2} \cdot s^{-1}$	2×10^{-11}	—	5×10^{-10}
L^m	μm	41	260	85
$brugg^f$	—	1.5	—	1.5
A^m	m^2	1.77×10^{-4}	1.77×10^{-4}	1.77×10^{-4}
$t_+{}^f$	—	0.363	0.363	0.363
$D_e{}^f$	$m^2 \cdot s^{-1}$	7.5×10^{-11}	7.5×10^{-11}	7.5×10^{-11}

α^f	—	0.5	—	0.5
$R_{film}{}^f$	$\Omega \cdot m^2$	0	—	—

For the upper subscript of the symbols, a represents adjustment, f represents reference, and m represents measurement.

Table 6. Parameters for cell equivalent circuit model

Symbol	Units	Value
R_{p1}	$\Omega \cdot m^{-2}$	4.74
C_{p1}	$F \cdot m^{-2}$	66.40
R_{p2}	$\Omega \cdot m^{-2}$	3.89
C_{p2}	$F \cdot m^{-2}$	38.00
R_0	$\Omega \cdot m^{-2}$	8.13

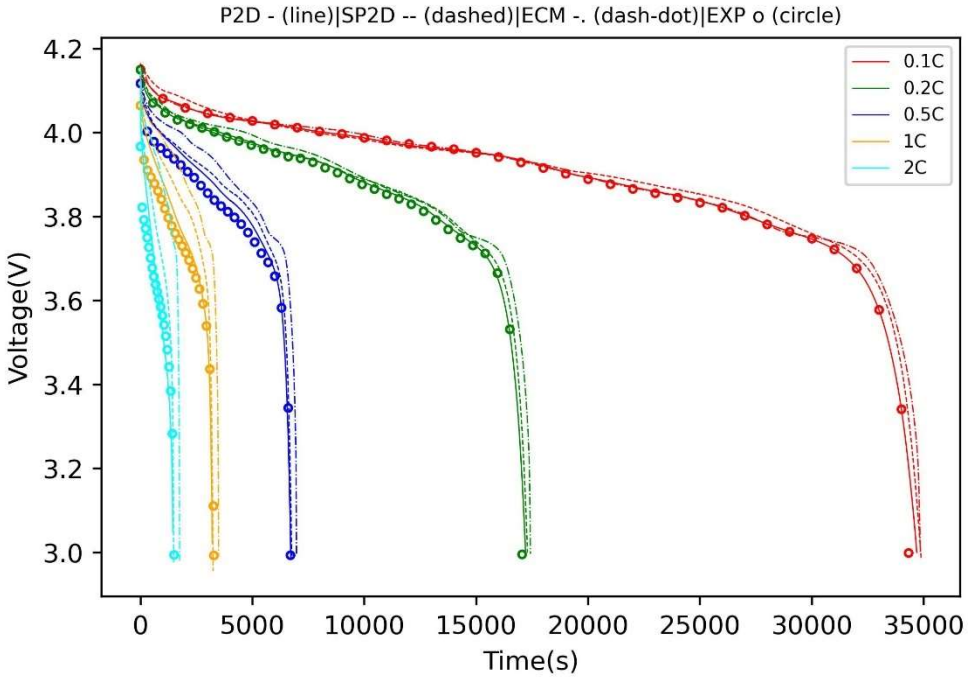

Figure 10. Comparison of P2D model, SP2D model, ECM model and experiment for 3.01 mAh LMO coin cell discharging at 0.1, 0.2, 0.5, 1 and 2 C -rates.

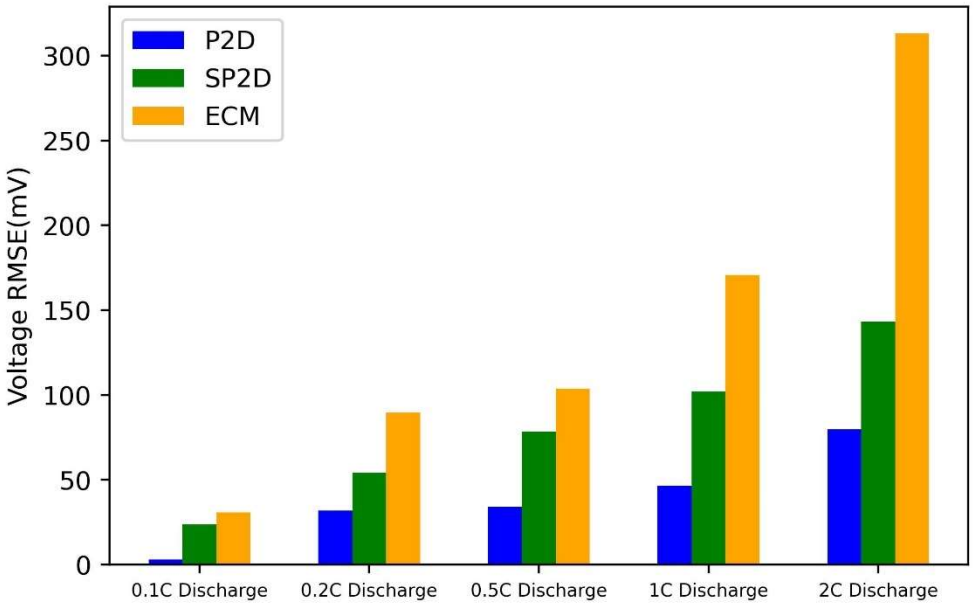

Figure 11. Root mean square error (RMSE) of three models at five C-rates relative to experimental data for 3.01 mAh LMO coin cell.

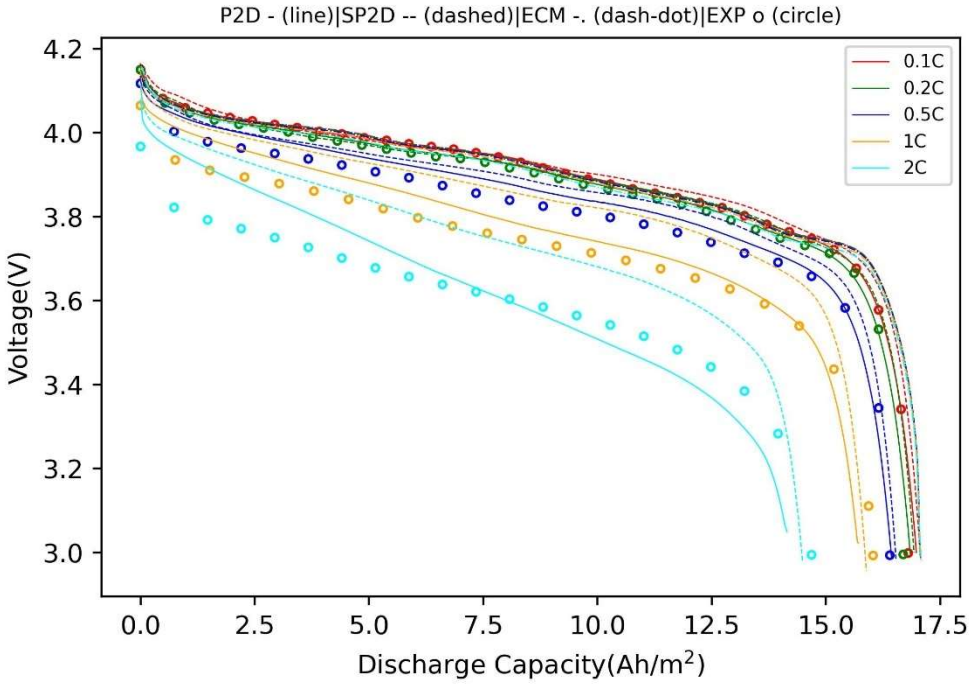

Figure 12. Rate capability test (voltage vs. discharge capacity) of three models compared to experimental data for 0.1, 0.2, 0.5, 1 and 2C discharge rates.

III. SOC Estimation Comparison

In this section, we estimate the SOC of the cell by dynamically testing a 10 Ah prismatic LMO cell using (Federal Urban Driving Schedule) FUDS condition. **Figure 13** shows the applied current of the cell. The predicted voltages for the SP2D model and the ECM and the measured voltage are shown in **Figure 14**. As the time increases, the voltage difference between the ECM and SP2D models is gradually amplified due to the larger polarization that the cell experiences as time progresses. The magnification box shows that the voltage curve of the SP2D model is closer to the experimental voltage curve. **Figure 15** shows the absolute error between the two models and the experimental voltage. We can see that the absolute error of the SP2D model is smaller than that of the ECM, which indicates that the SP2D model is also more accurate than the ECM under dynamic operating conditions. Besides, the absolute error of ECM tends to increase, but this phenomenon is not obvious for the SP2D model. This indicates that the accuracy of the ECM model decreases with time, while the accuracy of the SP2D model is no affected by time.

Next, we want to compare the cell SOC estimation results of different methods. The deep learning algorithm is built and trained in Python. The results of predicting SOC error by Bi-GRU network are shown in **Figure 16**. The accuracy of the SOC error prediction is 98%. The SOC comparison of EXP, Ampere-Hour, ECM+EKF, SP2D and SP2D+Bi-GRU are shown in **Figure 17**. The SOC curve based on SP2D + Bi-GRU almost overlaps with the experimental curve, while the SOC curve based on Ampere-Hour is the furthest from the experimental curve. At around 17500 s, the SOC curve based on ECM + EKF shows a drastic oscillation because the input data is fluctuating greatly during this time which leads to the instability of the EKF algorithm. **Figure 18** shows the absolute SOC errors for all four methods. For the Ampere-Hour method, the estimation error increases with time, which makes the SOC estimation result distorted after several cycles. For ECM+EKF, although the error is unstable, it has the benefit that the error can be kept within a certain range by filtering. For SP2D, it has the same problem as the Ampere-hour method, but with a relatively small error. For SP2D+Bi-GRU, it is clear that the SOC error is stable and almost zero. **Table 7** shows the quantitative analysis to evaluate the errors of the four methods. No matter which evaluation criteria are used, the SP2D+Bi-GRU method is the best. The estimation accuracy of this method reaches 99.97%, and the maximum absolute value of error is

0.001.

Table 7. Cell SOC estimation score

Method / Score	Ampere-Hour	ECM+EKF	SP2D	SP2D+BiGRU
$RMSE$	5.975	3.029	1.145	0.031
MAE	0.037	0.019	0.007	0.0001
MAX	0.072	0.045	0.015	0.001
$MRSD(\%)$	24.485	7.931	4.891	0.027

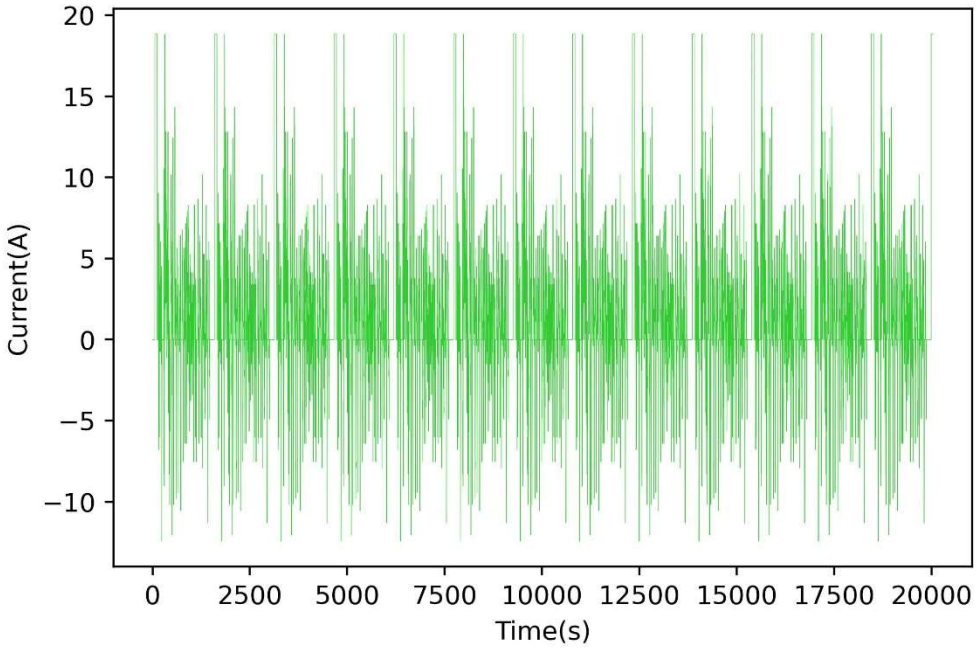

Figure 13. Applied current of FUDS as a function of time.

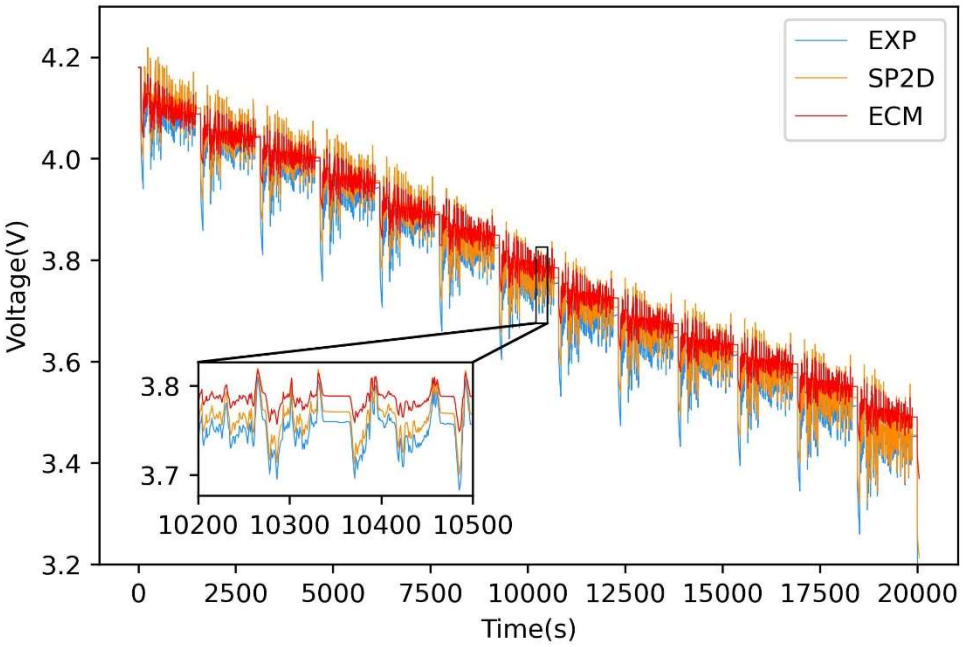

Figure 14. A comparison of predicted voltage of SP2D model, and ECM and experimentally measured voltage as a function of time for a current profile shown in Figure 13.

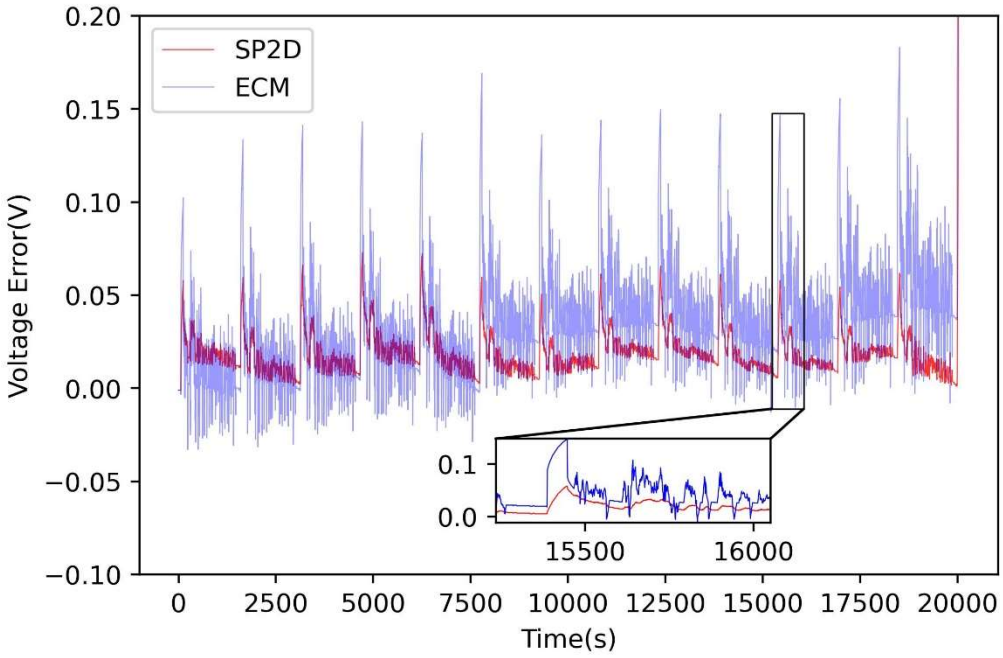

Figure 15. Voltage absolute error for SP2D model and ECM

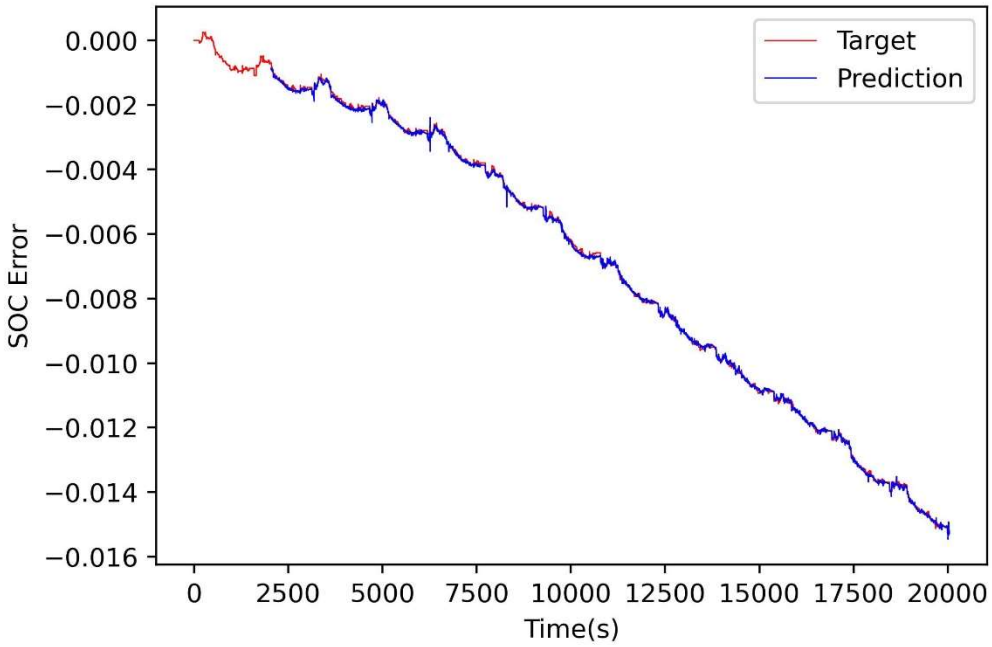

Figure 16. Prediction and target SOC error of Bi-GRU based on SP2D model.

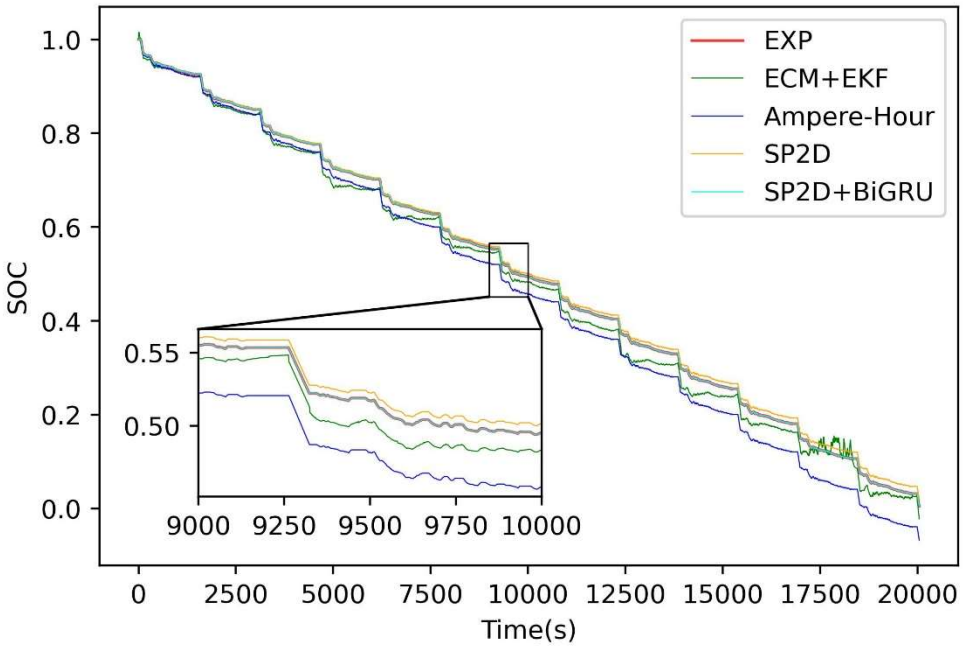

Figure 17. Comparison of SOC based on four different estimation methods and experimental data.

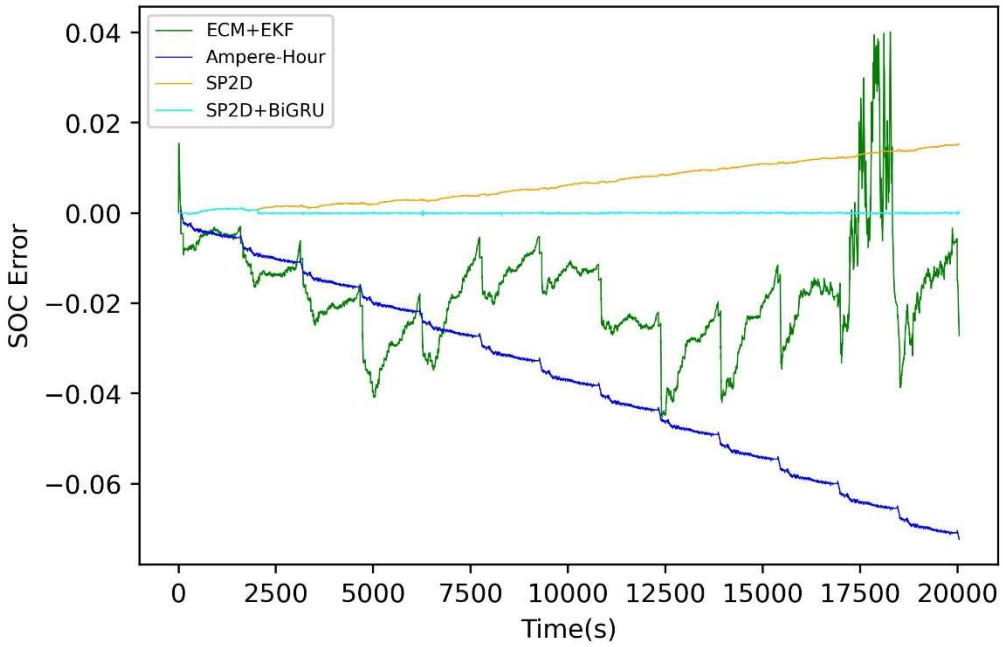

Figure 18. SOC absolute error for four different estimation methods.

Conclusion

In this work, we have proposed a method to predict the cell SOC. For this purpose, we used a framework that combines simplified electrochemical model with Bi-directional gated recurrent unit network, which has been proven to be a promising strategy for estimating the battery SOC in the cloud. This framework not only effectively improves the accuracy of the SOC estimation in the engineering field, but also helps researchers to understand the electrochemical mechanism during battery operation, which provides a feasible solution for implementing a cloud digital twin model of the battery in the future. In this paper, we evaluated the proposed framework from both model and estimation method perspectives and obtain the following conclusions: 1) The relative standard deviation of the SP2D model to the P2D model is less than 5%, which is mainly attributed to the distortion of the liquid phase lithium concentration. 2) The accuracy of the SP2D model is higher than that of the ECM model and lower than that of the SP2D model. 3) The accuracy of the SOC estimation based on the proposed framework is higher than that of the ampere hour integral method, the EKF method based on ECM, and the particle surface utilization method based on SP2D. The weaknesses of this framework come from the inaccurate parameters' adjustment of the

electrochemical model and requiring a large amount of data to train the algorithm. There are several directions that can be considered in this research in the future to further upgrade the proposed framework. We list some of them here. First, the SP2D model can be coupled with a thermal model and an aging model since the battery is subject to thermal and aging effects during real use. Second, advanced algorithms should be designed to accurately identify the electrochemical parameters in order to improve the simulation capability of the model. Third, obtaining more high-quality data for each type of cell, not only limited to current and voltage, helps improve the general performance of the algorithm.

References

1. D. Gielen, F. Boshell, D. Saygin, M.D. Bazilian, N. Wagner, R. Gorini, *Energy Strateg. Rev.*, 24 (2019) 38–50.
2. B. Diouf, R. Pode, *Renew. Energy*, 76 (2015) 375–380.
3. M.A. Hannan, M.M. Hoque, A. Hussain, Y. Yusof, P.J. Ker, *IEEE Access*, 6 (2018) 19362–19378.
4. K.W. See, G. Wang, Y. Zhang, Y. Wang, L. Meng, X. Gu, N. Zhang, K.C. Lim, L. Zhao, B. Xie, *Int. J. Coal Sci. Technol.*, 9 (2022).
5. D. Ouyang, J. Weng, M. Chen, J. Wang, Z. Wang, *J. Energy Storage*, 52 (2022) 104997.
6. G. T, D. C, *Electronics*, 11 (2022) 1795.
7. J. Meng, M. Ricco, G. Luo, M. Swierczynski, D.I. Stroe, A.I. Stroe, R. Teodorescu, *IEEE Trans. Ind. Appl.*, 54 (2018) 1583–1591.
8. S. Tamilselvi, S. Gunasundari, N. Karuppiah, A. Razak Rk, S. Madhusudan, V.M. Nagarajan, T. Sathish, M.Z.M. Shamim, C.A. Saleel, A. Afzal, *Sustain.*, 13 (2021) 1–26.
9. U. Krewer, F. Röder, E. Harinath, R.D. Braatz, B. Bedürftig, R. Findeisen, *J. Electrochem. Soc.*, 165 (2018) A3656–A3673.
10. A. Jokar, B. Rajabloo, M. Désilets, M. Lacroix, *J. Power Sources*, 327 (2016) 44–55.
11. M. Guo, X. Jin, R.E. White, *J. Electrochem. Soc.*, 164 (2017) A3602–A3613.
12. S. Santhanagopalan, Q. Guo, P. Ramadass, R.E. White, *J. Power Sources*, 156 (2006) 620–628.
13. S. Yuan, L. Jiang, C. Yin, H. Wu, X. Zhang, *J. Power Sources*, 352 (2017) 245–257.
14. M. Dubarry, B.Y. Liaw, *J. Power Sources*, 174 (2007) 856–860.
15. B.Y. Liaw, G. Nagasubramanian, R.G. Jungst, D.H. Doughty, *Solid State Ionics*, 175 (2004) 835–839.

16. S. Li, J. Li, H. He, H. Wang, *Energy Procedia*, 159 (2019) 168–173.

17. W. Zhou, Y. Zheng, Z. Pan, Q. Lu, *Processes*, 9 (2021).

18. I. Snihir, W. Rey, E. Verbitskiy, A. Belfadhel-Ayeb, P.H.L. Notten, *J. Power Sources*, 159 (2006) 1484–1487.

19. M. Gholizadeh, A. Yazdizadeh, *IET Electr. Syst. Transp.*, 9 (2019) 1–7.

20. M. Mastali, J. Vazquez-Arenas, R. Fraser, M. Fowler, S. Afshar, M. Stevens, *J. Power Sources*, 239 (2013) 294–307.

21. Z. Cui, W. Hu, G. Zhang, Z. Zhang, Z. Chen, *Energy Reports*, 8 (2022) 81–87.

22. H. He, H. Qin, X. Sun, Y. Shui, *Energies*, 6 (2013) 5088–5100.

23. C. Speltino, D. Di Domenico, G. Fiengo, A. Stefanopoulou, *2009 Eur. Control Conf. ECC 2009* (2014) 4828–4833.

24. D.N.T. How, M.A. Hannan, M.S. Hossain Lipu, P.J. Ker, *IEEE Access*, 7 (2019) 136116–136136.

25. G.Q. Qiu, W.M. Zhao, G.Y. Xiong, *Proc. 2018 Chinese Autom. Congr. CAC 2018* (2019) 91–96.

26. J.C. Alvarez Anton, P.J. Garcia Nieto, C. Blanco Viejo, J.A. Vilan Vilan, *IEEE Trans. Power Electron.*, 28 (2013) 5919–5926.

27. D.W. Chung, J.H. Ko, K.Y. Yoon, *J. Electr. Eng. Technol.*, 17 (2022) 1931–1945.

28. Z. Cui, L. Kang, L. Li, L. Wang, K. Wang, *Energy*, 259 (2022) 124933.

29. L.B. Using, M. Long, 100 (2021) 1–19.

30. M. Doyle, T.F. Fuller, J. Newman, *J. Electrochem. Soc.*, 140 (1993) 1526–1533.

31. K. Duru, P. Venkatachalam, C. Karra, A. Anish Madhavan, K. Elumalai, S. Kalluri, *ECS Trans.*, 107 (2022) 7485–7500.

32. J.L. Lee, A. Chemistruck, G.L. Plett, *J. Power Sources*, 220 (2012) 430–448.

33. X. Zhang, J. Lu, S. Yuan, J. Yang, X. Zhou, *J. Power Sources*, 345 (2017) 21–29

Appendix

Appendix A. Symbol Meaning

Symbol	Meaning
$C_{s,i}$	Solid phase lithium concentration
C_e	Electrolyte lithium concentration
$\varphi_{s,i}$	Solid phase potential
φ_e	Electrolyte potential
$D_{e,i}^{eff}$	Effective electrolyte diffusivity
σ_i^{eff}	Effective solid phase conductivity
K_i^{eff}	Effective electrolyte conductivity
η_i	Kinetic overpotential
$C_{e,0}$	Initial electrolyte concentration
$C_{s,0}$	Initial solid phase lithium concentration
$C_{s,i,surf}$	Particle surface lithium concentration
$C_{s,i,max}$	Particle maximum lithium concentration
α_a	Anode transfer coefficient
α_c	Cathode transfer coefficient
$D_{s,i}$	Solid-phase lithium diffusivity
D_e	Electrolyte diffusivity
k_i	Reaction rate constant
$\varepsilon_{e,i}$	Liquid phase volume fraction
$\varepsilon_{s,i}$	Solid phase volume fraction
t_+	Transport number
$Brugg$	Bruggeman factor
σ_i	Solid phase conductivity
K_i	Electrolyte conductivity
L_n	Thickness of anode
L_p	Thickness of cathode
L_s	Thickness of separator
$R_{s,i}$	Particle Radius
$j_{f,i}$	Volumetric current density
$a_{s,i}$	Particle relative surface area
F	Faraday constant
A	Area of electrode
R	Ideal gas constant
T	Temperature
R_{film}	Resistance of SEI film

I	Applied current
V	Output voltage
$U_{ocv,i}$	Open circuit voltage
r	Radial axis
x	Thickness axis
t	Time
i	Anode/Cathode
C	C-rate

Appendix B. SP2D Model in MATLAB/Simulink

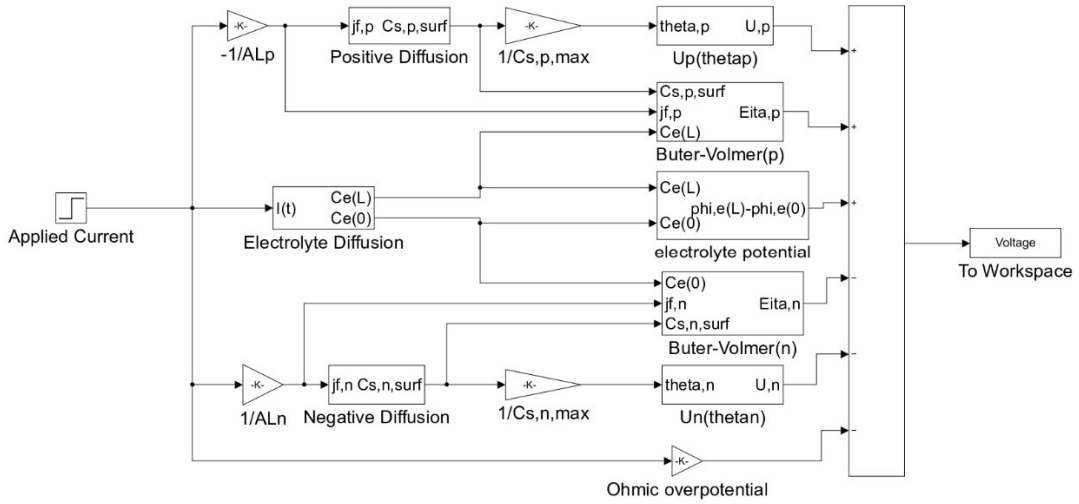

Appendix C. Parameter identification for ECM

For the equivalent circuit model, the Forgetting Factor-Recursive Least Squares algorithm (FF-RLS) can be used to identify the parameters C_{p1}, R_{p1}, C_{p2}, R_{p2}, R_0.

Step 1: Laplace transform of Eq.(30) *and discretization:*

$$U_{ocv}(s) = \left(\frac{R_{p1}}{\tau_1 s + 1} + \frac{R_{p2}}{\tau_2 s + 1} + R_0\right) I(s) + V(s)$$

Where, $\tau_1 = R_{p1}C_{p1}$ and $\tau_2 = R_{p2}C_{p2}$

$$s = \frac{[x(k) - x(k-1)]}{T} \quad s^2 = \frac{[x(k) - 2x(k-1) + x(k-2)]}{T^2}$$

Let $a = \tau_1\tau_2 \;\; b = \tau_1 + \tau_2 \;\; c = R_{p1}\tau_2 + R_{p2}\tau_1 + R_0(\tau_1 + \tau_2)\; d = R_0 + R_{p1} + R_{p2}$

$$U_{ocv}(k) - V(k) = k_1[U_{ocv}(k-1) - V(k-1)] +$$

$$k_2[U_{ocv}(k-2) - V(k-2)] + k_3 I(k) + k_4 I(k-1) + k_5 I(k-2)$$

$$k_1 = \frac{2a + bT}{a + bT + T^2} \quad k_2 = \frac{-a}{a + bT + T^2} \quad k_3 = \frac{aR_0 + cT + dT^2}{a + bT + T^2}$$

$$k_4 = \frac{-2aR_0 - cT}{a + bT + T^2} \quad k_5 = \frac{aR_0}{a + bT + T^2}$$

Define: $U_d(k) = U_{ocv}(k) - V(k)$

$$\varphi_k = [U_d(k-1) \quad U_d(k-2) \quad I(k) \quad I(k-1) \quad I(k-2)]^T$$

$$\theta_k = [k_1(k) \quad k_2(k) \quad k_3(k) \quad k_4(k) \quad k_5(k)]^T$$

Step 2: FF-RLS Algorithm

θ_k in Eq. can be solved by RLS algorithm, forgetting factor $\lambda = [0.95, 1]$.

$$\begin{cases} K_{k+1} = \dfrac{P_k\varphi_{k+1}}{\lambda + {\varphi_{k+1}}^T P_k \varphi_{k+1}} \\ P_{k+1} = \lambda^{-1}(P_k - K_{k+1}{\varphi_{k+1}}^T P_k) \\ \theta_{k+1} = \theta_k + K_{k+1}(U_d(k+1) - {\varphi_{k+1}}^T\theta_k) \end{cases}$$

Step 3: Identify R and C Parameters

Based on calculated θ_k, parameter C_{p1}, R_{p1}, C_{p2}, R_{p2}, R_0 will be identified.

$$k_0 = \frac{T^2}{1 - (k_1 + k_2)} \quad a = -k_0 k_2 \quad b = \frac{k_0(k_1 + 2k_2)}{T} \quad c = \frac{-k_0(k_4 + 2k_5)}{T}$$

$$d = \frac{k_0(k_3 + k_4 + k_5)}{T^2} \quad R_0 = -\frac{k_5}{k_2}$$

$$\begin{cases} R_0 = -\dfrac{k_5}{k_2} \\ \tau_1 = \dfrac{b + \sqrt{b^2 - 4a}}{2} \\ \tau_2 = \dfrac{b - \sqrt{b^2 - 4a}}{2} \\ R_{p1} = \dfrac{c - \tau_1 d - R_0 \tau_2}{\tau_2 - \tau_1} \\ R_{p2} = d - R_{p1} - R_0 \\ C_{p1} = \dfrac{\tau_1}{R_{p1}} \\ C_{p2} = \dfrac{\tau_2}{R_{p2}} \end{cases}$$